short communications

Feasibility study of interferometric phase-contrast X-ray imaging using the hard-X-ray free-electron laser of the SPring-8 Angstrom Compact Free-Electron Laser

Akio Yoneyama,[a]* Rika Baba,[a] Daiko Takamatsu,[a] Chika Kamezawa,[b] Ichiro Inoue,[c] Taito Osaka,[c] Shigeki Owada[d] and Makina Yabashi[c]

[a]Research and Development Group, Hitachi Ltd., 1-280 Higashi-koigakubo, Kokubunji, Tokyo 185-8601, Japan, [b]Department of Materials Structure Science, The Graduate University for Advanced Studies, 1-1 Oho, Tsukuba, Ibaraki 305-0801, Japan, [c]RIKEN SPring-8 Center, 1-1-1 Kouto, Sayo-cho, Sayo-gun, Hyogo 679-5148, Japan, and [d]Japan Synchrotron Radiation Research Institute, 1-1-1 Kouto, Sayo-cho, Sayo-gun, Hyogo 679-5198, Japan. *Correspondence e-mail: akio.yoneyama.bu@hitachi.com

Aiming for the fine observation of fast physical phenomena such as phonon propagation and laser ablation, phase-contrast X-ray imaging combined with a crystal X-ray interferometer and the X-ray free-electron laser (XFEL) of the SPring-8 Angstrom Compact Free-Electron Laser has been developed. An interference pattern with 70% visibility was obtained by single-shot exposure with a 15 keV monochromated XFEL. In addition, a phase map of an acrylic wedge was successfully obtained using the fringe scanning method.

1. Introduction

Phase-contrast X-ray imaging using a crystal X-ray interferometer (XI) (Bonse & Hart, 1965; Momose et al., 1996) has the highest sensitivity among phase-sensitive X-ray imaging methods (Yoneyama et al., 2008, 2015), and the density resolution of three-dimensional observation can reach 0.5 mg cm^{-3} (Yoneyama et al., 2013). We have studied many biological samples, for example soft tissues such as the kidney, brain and heart (Takeda et al., 2002; Yoneyama et al., 2005; Noda-Saita et al., 2006), embryos (Yamada et al., 2012), energy materials such as methane hydrates (Takeya et al., 2006), and industrial products such as lithium ion batteries (Takamatsu et al., 2018), achieved by taking advantage of the high sensitivity of XI. In addition, we developed X-ray thermography (Yoneyama et al., 2018) for detecting changes in temperature caused by thermal expansion, and we successfully performed time-resolved observation of thermal flow in heated water with a 1.3 s interval.

The high sensitivity of the method motivated us to use it in combination with XFELs for extremely fast time-resolved phase-contrast X-ray imaging. The pulse length of an XFEL is less than 10 fs; therefore, fine observation of very fast physical phenomena such as phonon propagation and laser ablation is expected. For the first step of developing fast XI with XFELs, we performed a feasibility study which involved the generation of X-ray interference patterns and obtained a phase map using the fringe scanning method.

2. Method and instrumentation

The feasibility study was performed at BL3 of the SPring-8 Angstrom Compact Free-Electron Laser (SACLA), Japan,

XFEL
Phase shifter
Interference beams
X-ray camera
Sample
α
Monolithic LLL
X-ray interferometer
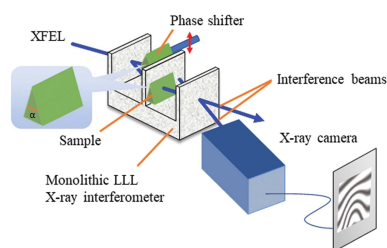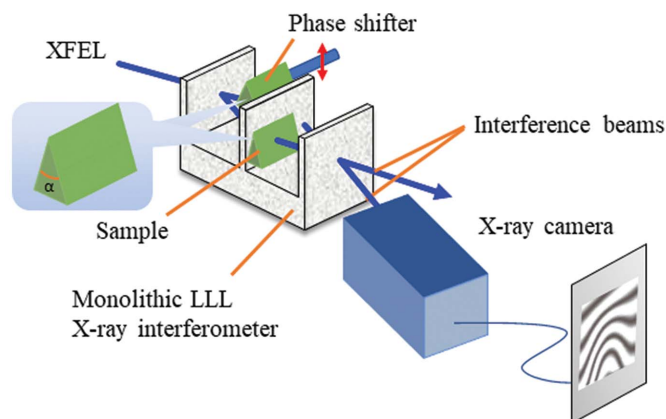
Figure 1
Schematic view of the experimental setup for the feasibility study. A monolithic triple-Laue (LLL) crystal X-ray interferometer was used.

using the experimental setup shown in Fig. 1. The XFEL beam was monochromated by a double-crystal monochromator using Si(111) and inputted to a monolithic triple-Laue (LLL) crystal X-ray interferometer (Bonse & Hart, 1965). The beam was divided, reflected and recombined by the splitter-, mirror- and analyzer-crystal wafers of the interferometer, respectively, using Laue-case (220) diffraction of silicon. One of the generated interference beams (H-waves) was detected by an X-ray camera.

The interferometer was positioned using a high-precision rotational positioning table with a tangential bar to stabilize the incident angle of the XFEL beam. The X-ray interferometer was cut monolithically from a perfect silicon crystal ingot. The thickness of the crystal wafers was 1 mm, and the interval between the wafers was 15 mm. The coherent length and the beam divergence of the XFEL beam had almost the same values in the vertical and horizontal directions, so the interferometer was set horizontally to keep the mechanical stability high and avoid the influence of gravity. The whole interferometer was covered with an acrylic case to suppress the phase fluctuation caused by air flow around the interferometer.

The X-ray camera consists of a scintillator [10 μm LSO (Lu_2SiO_5:Ce)] that converts X-rays to visible light, a relay lens system that transmits the visible light and a CMOS (Hamamatsu, C11440-22C) that detects visible light. The magnification of the lens system was 10×, and the effective pixel size was 0.65 μm. The number of pixels was 2048 × 2048, and the field of view was 1.3 mm × 1.3 mm. The frame rate was faster than 50 frames s^{-1}, and every image could be taken with a single shot of the XFEL beam.

3. Results

3.1. X-ray interference pattern

Fig. 2(*a*) shows an interference pattern and the average vertical line profile of a blue rectangle (10 pixels wide) obtained by a single-shot exposure achieved using a monochromated 15 keV XFEL beam. The intensity and spatial
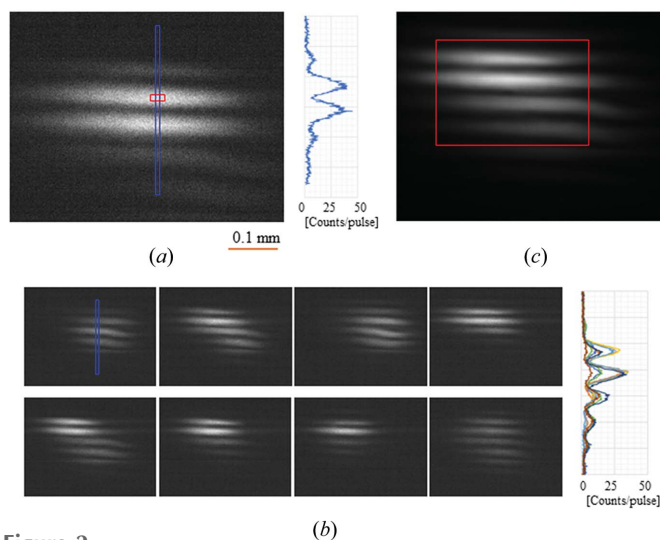
Figure 2
(*a*) X-ray interference pattern and line profile obtained from a single shot of the monochromatic 15 keV XFEL beam. (*b*) Series of interference patterns and line profiles obtained from single-shot exposures carried out continuously. The peak position of fringes was fixed despite the variation in intensity and spatial distribution shot-by-shot. (*c*) Interference pattern obtained from a 10 s exposure (300 shots). A visibility of 60% was obtained despite the addition of 300 shots.

distribution of the area of strong intensity of the XFEL changed greatly shot-by-shot, and the pattern with the highest interference intensity was selected and is shown in Fig. 2(*a*). None of the crystal wafers of the interferometer had any crystal distortion, and the interference beams formed a uniform intensity without any objects in the object beam and reference beam paths. A wedge plate made of acrylic resin with an acute angle (α = 45°) was placed vertically in the reference beam path to generate interference fringes for easy determination of the visibility by one-shot exposure.

The visibility of the interference pattern in Fig. 2(*a*) was calculated at 70%, and the maximum visibility was 60% using the same X-ray interferometer at SPring-8 and the SAGA Light Source (conventional synchrotron facilities). The same visibility (60%) was obtained, although at different exposure times; therefore, it was assumed that the decrease in visibility was caused by the shape error of the interferometer. The beam paths of the object and reference in the interferometer deviated and did not meet at the same point on the analyzer crystal due to the shape error, and the visibility decreased because conventional synchrotron radiation X-rays have a short coherent length. The coherent length of an XFEL is long enough, and the influence of the shape error does not affect the visibility, hence a high visibility (70%) was obtained.

Fig. 2(*b*) shows a series of interference patterns and vertical line profiles obtained by single-shot exposures collected continuously (30 Hz). The spatial distribution of the area of strong intensity changed shot-by-shot; however, the fringe pattern remained at the same position as shown in the line profiles. Fig. 2(*c*) shows interference patterns obtained from a 10 s exposure (300 shots). As expected from Fig. 2(*b*), a high visibility of 60% was obtained despite the addition of 300 shots because of the high stability of the phase shift. These

results show that methods can be used which require multiple interference patterns to obtain phase maps (spatial distribution of phase shifts caused by samples) such as the fringe scanning method.

The detected maximum camera signal in the constructive interference region indicated in the red square in Fig. 2(a) was 35 counts per shot per pixel, and the average camera signal in the red square in Fig. 2(c) was 10 counts per shot per pixel. The average X-ray photon flux of the interference beam at the front of the X-ray camera was calculated to be 8.3×10^8 photons per shot from the measured average 15 keV XFEL pulse energy (3.2 µJ), the transmittance of the X-ray interferometer [1.5% for three Si crystal wafers of 1 mm thickness × 2 (the object and reference beams)], and absorption by air between the exit port of the beamline and the X-ray camera, the polyimide film of the cover for the X-ray interferometer and the wedge plate (50%). The interference beam size was 0.5 mm × 0.35 mm and the pixel size of the camera was 0.65 µm × 0.65 µm; therefore, the number of X-ray photons was calculated at 31 counts per pixel. The conversion efficiency – from X-ray to the camera signal – of the camera [Hamamatsu, high-resolution X-ray imaging system (M11427-51)] was estimated to be 35% from the absorption of the scintillator for 15 keV X-rays [45% for 10 µm LSO (Lu_2SiO_5:Ce)], the conversion ratio from X-ray to visible light of the scintillator [~240 visible-light photons per X-ray photon (Spurrier *et al.*, 2008; Chewpraditkul *et al.*, 2009)], the numerical aperture (NA = 0.3) of the objective lens, and the quantum efficiency (45% for 420 nm) of the sCMOS camera (Hamamatsu, C11440-22C). Therefore, the camera signal was calculated at 11 counts per shot per pixel, which corresponds reasonably to the detected value. The standard deviation of the camera signal in the red square of Fig. 2(a) was 10 counts. The quantum noise was calculated at about 6 counts; therefore, the rest of the noise could be attributed to the readout noise of the sCMOS camera.

3.2. Phase map

As a next step, we observed the phase map of a test sample using the fringe scanning method (Bruning *et al.*, 1974). Two wedge plates made of acrylic resin were placed vertically in the object beam and reference beam paths as a sample and phase shifter, respectively. The space for the phase shifter of the reference beam path was restricted to a small area, and a wedge plate with a large acute angle ($\alpha = 60°$) was used as a phase shifter to suppress the vertical movement for phase-shifting. A sample wedge plate with an acute angle ($\alpha = 26.5°$) was placed in the object beam path in the same direction as the phase shifter as shown in Fig. 1.

(a)

(b)
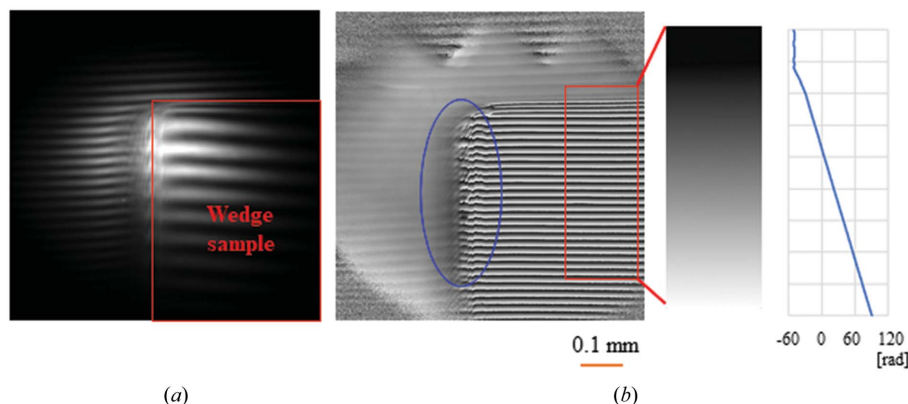
Figure 3
(a) Interference pattern. (b) Phase map with the background phase subtracted, unwrapped phase map and line profile of a wedge made of acrylic resin. Blurring of the left side of the wedge (indicated by the blue ellipse) was caused by the Bormann fan effect in the analyzer-crystal wafer.

Fig. 3(a) shows the interference pattern obtained with a 10 s exposure time (300 shots). The interference fringe spacing in the background area was smaller than that of the pattern in Fig. 2(a) because of the large angle of the wedge. In addition, the fringe spacing in the sample area was wider than that in the background area because the phase shifts caused by the sample and phase shifter were cancelled by placing them in the same direction as the wedge.

Fig. 3(b) shows the phase map with the background phase subtracted, an unwrapped phase map of a part of the sample wedge and a line profile of the unwrapped phase map obtained by 13-step fringe scanning. The exposure time of each interference pattern was 10 s (300 shots), and the total measurement time was 150 s including the operating time for moving the phase shifter. A fine phase map of the sample, similar to that obtained by conventional synchrotron radiation X-rays, was successfully obtained, despite the remaining small fringe-like artifacts caused by the intensity fluctuation of the XFEL. Blurring on the left side of the wedge (indicated by the blue ellipse) was caused by the Bormann fan effect in the analyzer-crystal wafer.

Phase unwrapping was performed correctly in the middle of the sample area, and the density of the sample was calculated at 1.15 g cm^{-3}, which coincides with the standard density of acrylic resin (1.18 g cm^{-3}) within 3%, from the phase shift and the incline of the sample. The phase fluctuation calculated from the standard deviation in the background area was 0.05 radians, which is similar to the value in phase-contrast X-ray imaging using conventional synchrotron radiation (Yoneyama *et al.*, 2013).

4. Conclusions

A feasibility study on phase-contrast X-ray imaging combined with a crystal X-ray interferometer and XFEL beam was performed at SACLA. X-ray interference pattern images with 70% visibility were obtained by single-shot exposures collected continuously with a 15 keV monochromated XFEL beam. The shape error of the X-ray interferometer used was small, and the visibility was only 10% higher than that

of images obtained at conventional synchrotron facilities. Therefore, the contribution of high coherence (long coherent length) of the XFEL was small for our study. On the other hand, triple Bragg (BBB) interferometers (Sutter *et al.*, 2004) and nonplanar three-beam interferometers (Yoneyama *et al.*, 2002), having large shape errors caused by difficult fabrication, are expected to be employed in phase-contrast imaging with XFELs, taking advantage of the long coherent length. In addition, the crystal-separated (two-crystal) X-ray interferometer (Yoneyama *et al.*, 2013) requires highly rigid positional tables for the operation to suppress phase fluctuation caused by mechanical vibrations. The beam exposure time was only 10 fs with the XFEL, and mechanical stability for the interferometer was not required. Therefore, various types of crystal X-ray interferometers which can be separated into multiple parts can be used without rigid positional tables.

A phase map of an acrylic wedge was successfully obtained with a 0.05 radian phase fluctuation using the fringe scanning method. X-ray thermography (Yoneyama *et al.*, 2018) using the crystal X-ray interferometer allows us to visualize thermal propagation in materials non-destructively by using slight density changes caused by thermal expansion. However, the time resolution is restricted to 1.3 s by the low photon flux of the conventional synchrotron radiation X-ray, and only slow thermal propagation in liquid can be visualized. The combination of pumping by pulse laser heating and probing by crystal interferometric phase-contrast imaging with an XFEL (as shown in Fig. 4) has the potential to break through this limitation so that thermal flow (phonon propagation) can be visualized in solid materials with a picosecond time resolution.

The obtained phase fluctuation of 0.05 radians corresponds to 30°C of aluminium foil 10 μm in thickness; hence, fine visualization of picosecond time-resolved thermal (phonon) propagation in solid materials is possible. In addition, single-shot phase imaging is possible by thinning the crystal wafers of the interferometer (Hirano & Momose, 1999) to increase the transmittance and by the Fourier sub-fringe method (Takeda *et al.*, 1982).

Figure 4
Schematic view of the pump and probe method combining laser heating (pump) and crystal interferometric phase-contrast imaging with an XFEL (probe) for detecting thermal propagation in solid samples.

References

Bonse, U. & Hart, M. (1965). *Appl. Phys. Lett.* **6**, 155–156.

Bruning, J. H., Herriott, D. R., Gallagher, J. E., Rosenfeld, D. P., White, A. D. & Brangaccio, D. J. (1974). *Appl. Opt.* **13**, 2693–2703.

Chewpraditkul, W., Swiderski, L., Moszynski, M., Szczesniak, T., Syntfeld-Kazuch, A., Wanarak, C. & Limsuwan, P. (2009). *IEEE Trans. Nucl. Sci.* **56**, 3800–3805.

Hirano, K. & Momose, A. (1999). *Jpn. J. Appl. Phys.* **38**, L1556–L1558.

Momose, A., Takeda, T., Itai, Y. & Hirano, K. (1996). *Nat. Med.* **2**, 473–475.

Noda-Saita, K., Yoneyama, A., Shitaka, Y., Hirai, Y., Terai, K., Wu, J., Takeda, T., Hyodo, K., Osakabe, N., Yamaguchi, T. & Okada, M. (2006). *Neuroscience*, **138**, 1205–1213.

Spurrier, M. A., Szupryczynski, P., Yang, K., Carey, A. A. & Melcher, C. L. (2008). *IEEE Trans. Nucl. Sci.* **55**, 1178–1182.

Sutter, J. P., Ishikawa, T., Kuetgens, U., Materlik, G., Nishino, Y., Rostomyan, A., Tamasaku, K. & Yabashi, M. (2004). *J. Synchrotron Rad.* **11**, 378–385.

Takamatsu, D., Yoneyama, A., Asari, Y. & Hirano, T. (2018). *J. Am. Chem. Soc.* **140**, 1608–1611.

Takeda, M., Ina, H. & Kobayashi, S. (1982). *J. Opt. Soc. Am.* **72**, 156.

Takeda, T., Momose, A., Wu, J., Yu, Q., Zeniya, T., Thet-Thet-Lwin, Yoneyama, A. & Itai, Y. (2002). *Circulation*, **105**, 1708–1712.

Takeya, S., Honda, K., Yoneyama, A., Hirai, Y., Okuyama, J., Hondoh, T., Hyodo, K. & Takeda, T. (2006). *Rev. Sci. Instrum.* **77**, 053705.

Yamada, S., Nakashima, T., Hirose, A., Yoneyama, A., Takeda, T. & Takakuwa, T. (2012). *Developmental Anatomy of the Human Embryo – 3D Imaging and Analytical Techniques*, in *The Human Embryo*, pp. 111–126. InTechOpen.

Yoneyama, A., Baba, R., Hyodo, K. & Takeda, T. (2015). *European Congress of Radiology (ECR 2015)*, 4–8 March 2015, Vienna, Austria. Poster C-0531.

Yoneyama, A., Iizuka, A., Fujii, T., Hyodo, K. & Hayakawa, J. (2018). *Sci. Rep.* **8**, 12674.

Yoneyama, A., Momose, A. & Koyama, I. (2002). *Jpn J. Appl. Phys.* **41**, L161–L163.

Yoneyama, A., Nambu, A., Ueda, K., Yamada, S., Takeya, S., Hyodo, K. & Takeda, T. (2013). *J. Phys. Conf. Ser.* **425**, 192007.

Yoneyama, A., Takeda, T., Tsuchiya, Y., Wu, J., Lwin, T.-T., Hyodo, K. & Hirai, Y. (2005). *J. Synchrotron Rad.* **12**, 534–536.

Yoneyama, A., Wu, J., Hyodo, K. & Takeda, T. (2008). *Med. Phys.* **35**, 4724–4734.